High aspect ratio grid effects on the accuracy of Navier–Stokes solutions on unstructured meshes

Aaron Katz *, Venkateswaran Sankaran

US Army Aeroflightdynamics Directorate (AMRDEC), Moffett Field, CA 94035, USA

ARTICLE INFO

ABSTRACT

The method of manufactured solutions is used to evaluate the stability and accuracy of several unstructured discretization schemes in the presence of high-aspect ratio grids. Both inviscid and viscous discretizations are studied by systematically varying parameters such as the aspect ratio, mesh stretching, curvature, skewness, and non-planar faces. For the inviscid terms, gradient reconstruction based on cell least squares and nodal Green–Gauss are considered. In particular, high curvature grids are shown to lead to instabilities with both classes of schemes and a new Green–Gauss scheme based on nodal projection is developed that retains stability and formal second-order accuracy under all conditions. A further advantage of the nodal Green–Gauss schemes is that the nodal values can be used in the viscous discretization as well. All the viscous schemes tested here are demonstrated to preserve second-order accuracy. Finally, for three-dimensional meshes, triangulation of non-planar faces is found to be necessary to preserve second-order accuracy.

1. Introduction

Unstructured grids have achieved mainstream use for computational fluid dynamics (CFDs) due to their ability to automatically discretize complex domains. Unstructured grids are often composed of a variety of elements including tetrahedra, hexahedra, prisms, and pyramids to efficiently capture features on a variety of length scales including boundary layers, shocks, and vortical features [1]. Because of the large variation in length scale, unstructured grids often exhibit a high degree of anisotropy and stretching for high Reynolds number flows. Additionally, geometric complexity may lead to grids with non-ideal mesh features, such as skewness and high levels of curvature. The focus of this paper is to systematically examine the solution accuracy and stability of unstructured grid schemes as a function of mesh parameters such as aspect ratio, stretching, curvature, and skewness.

The large body of research in recent years related to unstructured grid schemes is evidence of the significant challenges associated with these discretizations. An extensive overview of these schemes is given by Mavriplis [2]. Schemes are often classified by the location of the principal unknowns, either at the nodes or cell centers. Both node- and cell-centered schemes require extended stencils to perform gradient reconstruction for accuracy greater than first order. Memory requirements and computational

costs can become significant in the implementation of these schemes, often requiring tradeoffs between accuracy and computational effort. In addition to greater expense, extended stencils may lead to instability for certain mesh configurations due to poor gradient estimation or inexact Jacobian computation for implicit schemes. This difficulty was recognized by Holmes and Connell [3], who introduced the notion of "clipping" of the pseudo-Laplacian coefficients to increase stability and robustness for highly deformed meshes. Diskin and Thomas subsequently showed that accuracy suffered as a result of clipping [4]. Despite these and other difficulties, unstructured grid schemes have nonetheless proven successful at accommodating complex geometry using mixed element meshes for practical aerodynamics applications [5].

In order to quantify the accuracy of unstructured grid schemes precisely it is necessary to have exact solutions to the continuous equations. Non-trivial exact solutions for complex systems of equations are often difficult or impossible to obtain. For this reason, throughout this work we perform error studies using grid refinement and the method of manufactured solutions (MMSs) [6]. With MMS, a "manufactured" solution is arbitrarily prescribed first, after which an analytic source term is added to the original continuous equations such that the manufactured solution becomes an exact solution of the modified equation. MMS has achieved widespread use for code verification both as a means of detecting coding errors and to evaluate order of accuracy [7,8]. In addition, researchers have used the method to evaluate grid quality effects [9–11]. Likewise, in this work we use MMS to verify order of accuracy as well as the magnitude of solution errors for

* Corresponding author. Address: M/S 215-1, Ames Research Center, Moffett Field, CA 94035, USA. Tel.: +1 650 604 3697; fax: +1 650 604 5173.
E-mail address: akatz@merlin.arc.nasa.gov (A. Katz).

mesh and solution configurations of practical interest. In addition, the MMS procedure performed on a series of refined meshes also provides a means of assessing stability behavior of candidate schemes.

In this work, we extend our previous MMS-based analysis [12] specifically to examine high aspect ratio viscous flows using the Navier–Stokes equations. A major result of the previous studies was that cell-centered schemes, in particular prismatic cell-centered schemes, produced less error for anisotropic grids than node-centered schemes. We showed that the widely used median-dual node-centered approximation is second order accurate for general triangular (tetrahedral in 3D) grids, but reduces to first order for other cell types, including prisms, hexahedra, and pyramids [13]. These findings indicate that for anisotropic and mixed element grids, cell-centered approaches are preferred. For this reason, we primarily examine cell-centered prismatic discretizations in this work. Within this class of schemes, we have found that the most critical elements in the discretization process are the methods of reconstruction and flux integration. Accordingly, we examine a variety of gradient estimation methods, including constant, cell-least squares, and a variety of nodal Green–Gauss techniques. We also introduce a new nodal method designed to maintain second-order accuracy and stability for high aspect ratio grids and high curvature. The nodal methods are used directly in the viscous face gradient formulation. These schemes are evaluated systematically as a function of mesh parameters including aspect ratio, stretching, skewness, and curvature. Moreover, we evaluate methods of flux integration on non-planar faces, including single and double point quadrature on triangular facets. The overall goal of these studies is to identify schemes that produce the lowest levels of solution error while maintaining stability over a wide range of mesh features.

The paper is organized as follows: first, we present our computational approach, including details of the MMS procedure as well as spatial discretization schemes for inviscid and viscous terms. Various methods of gradient reconstruction are discussed along with methods to determine face gradients for viscous flux computation. Next we present detailed assessments of these algorithms for common mesh features. We systematically study the effects of aspect ratio, mesh stretching, curvature, skewness, and non-planar faces in three dimensions. Finally, we offer some conclusions regarding these methods and the grid refinement procedure itself.

2. Computational approach

In this work we are interested in solving systems of conservation laws of the form

$$\frac{\partial Q}{\partial t} + \nabla \cdot \boldsymbol{F} - \nabla \cdot \boldsymbol{F}_v = 0, \tag{1}$$

where Q represents a vector of conserved variables, t is physical time, $\boldsymbol{F} = F\hat{i} + G\hat{j} + H\hat{k}$ represents inviscid fluxes, and $\boldsymbol{F}_v = F_v\hat{i} + G_v\hat{j} + H_v\hat{k}$ represents viscous fluxes. We examine both a scalar model equation and the Navier–Stokes system of equations. For the scalar equation we use

$$\begin{aligned}
Q &= \phi, \\
F &= a\phi, \quad G = b\phi, \quad H = c\phi, \\
F_v &= v\frac{\partial \phi}{\partial x}, \quad G_v = v\frac{\partial \phi}{\partial y}, \quad H_v = v\frac{\partial \phi}{\partial z},
\end{aligned} \tag{2}$$

where ϕ represents a scalar quantity, a, b, and c represent constant wave speeds in each coordinate direction, and v represents the constant coefficient of diffusion. We may define a Reynolds number based on a reference length, l, and characteristic speed, $\tilde{a}$, as

$$Re_l = \frac{\tilde{a}l}{v}. \tag{3}$$

For high-aspect ratio cells or domains, the characteristic length of each coordinate direction can vary significantly leading to different Reynolds numbers for each direction.

The Navier–Stokes equations may be expressed as

$$Q = \begin{Bmatrix} \rho \\ \rho u \\ \rho v \\ \rho w \\ \rho e \end{Bmatrix},$$

$$F = \begin{Bmatrix} \rho u \\ \rho u^2 + P \\ \rho u v \\ \rho u w \\ \rho u h_0 \end{Bmatrix}, \quad G = \begin{Bmatrix} \rho v \\ \rho v u \\ \rho v^2 + p \\ \rho v w \\ \rho v h_0 \end{Bmatrix}, \quad H = \begin{Bmatrix} \rho w \\ \rho w u \\ \rho w v \\ \rho w^2 + P \\ \rho w h_0 \end{Bmatrix},$$

$$F_v = \begin{Bmatrix} 0 \\ \tau_{xx} \\ \tau_{xy} \\ \tau_{xz} \\ u_i\tau_{xi} - q_x \end{Bmatrix}, \quad G_v = \begin{Bmatrix} 0 \\ \tau_{yx} \\ \tau_{yy} \\ \tau_{yz} \\ u_i\tau_{yi} - q_y \end{Bmatrix}, \quad H_v = \begin{Bmatrix} 0 \\ \tau_{zx} \\ \tau_{zy} \\ \tau_{zz} \\ u_i\tau_{zi} - q_z \end{Bmatrix}, \tag{4}$$

where ρ, u, v, w, e, h_0, and P represent density, the Cartesian velocity components, total energy, total enthalpy, and pressure, respectively. Also, τ and $\boldsymbol{q}$ represent the viscous stress tensor and heat flux vectors. The Reynolds number for the Navier–Stokes equations we define as

$$Re_l = \frac{\rho U l}{\mu}, \tag{5}$$

where U is a characteristic velocity, and μ is the dynamic viscosity.

We desire to discretize the above equations on unstructured grids and compute the resulting error. One common misunderstanding in error analysis for unstructured grid schemes stems from the difference between truncation error and solution error. The two types of error do not necessarily converge at the same rate, a fact which has sometimes led to confusion [9,11]. Truncation error may be defined as the residual present when an exact solution is introduced into a discretization. For example, consider a discretization of a linear equation, such as the one in Eq. (2) at steady state. If known Dirichlet conditions Q_b are supplied at some boundary values, a linear discretization may be expressed as

$$DQ^h = BQ_b, \tag{6}$$

where D represents the discrete scheme operating on the discrete solution, Q^h, and B incorporates the Dirichlet conditions. Note that the discrete solution exactly satisfies the system of equations while the exact solution, Q, applied to the discrete equations yields an error

$$DQ = BQ_b + E_t, \tag{7}$$

where E_t is the truncation error.

On the other hand, the solution error is defined as the difference between the exact and discrete solutions. Using the above definitions, we can relate the solution error to the truncation error by

$$E_s = Q - Q^h = D^{-1}E_t, \tag{8}$$

or

$$DE_s = E_t. \tag{9}$$

The solution error is assumed to be dominated by terms of leading order p such that

$$E_s = Q - Q^h = K\Delta h^p + HOT, \tag{10}$$

where K consists of constants independent of the mesh size, h, and *HOT.* stands for high order terms.

While this result is restricted to linear equations, it serves to highlight the difference between truncation error and solution error. Eq. (9) shows that the solution error is a solution to the discrete equations governing Q when driven by the local truncation error as a source term. Our previous studies, as well as those of other researchers, have shown that the order of convergence of solution error is often not the same as the order convergence of truncation error for finite volume schemes [12,14–16]. Therefore, truncation error for finite volume schemes does not yield a reliable estimate of the order of accuracy. We must actually solve the system of equations to determine the solution error, which is of primary interest.

To compute the solution error, exact solutions are required. Most exact solutions for coupled systems of equations are quite simple and may not even engage all the terms in the governing equations. To address this problem, Roache [6] proposed the Method of Manufactured Solutions, or MMS. Here, instead of solving Eq. (1) directly, we solve the equation augmented with an analytic source term

$$\frac{\partial Q}{\partial t} + \nabla \cdot \boldsymbol{F} - \nabla \cdot \boldsymbol{F}_v = S. \tag{11}$$

The MMS procedure involves selecting an arbitrary "manufactured" solution and then substituting the manufactured solution into the original continuous differential equation. The manufactured solution will not in general identically satisfy the differential equation, and the remainder is set equal to the source term [8]. Thereby, the manufactured solution represents the exact solution of the modified continuous differential equation, i.e., the original equation with the source term added. We note that the source term is not a function of Q, but is only a function of the independent variables and parameters of the PDE. Careful treatment of the source term in a manner consistent with the overall discretization method appears to be critical to obtaining accurate error estimates [12,7]. Specifically, the source term should be discretized to the same order of accuracy or greater than the terms in the original PDE. In this work, we examine second order accurate algorithms. While we tested higher order accurate discretizations for the source term, little difference could be seen over a second order accurate source term discretization. Therefore, all results presented use second order accurate source term discretizations.

3. Discretization schemes

3.1. Inviscid terms

The previous section addressed issues of solution error quantification for the discretization of complex systems of equations. In this section, we examine the details of several discretization schemes for inviscid terms using a cell-centered approach. Using a finite volume formulation, the spatial discretization for the inviscid terms in Eq. (1) may be expressed as

$$\nabla \cdot \boldsymbol{F}(Q) \approx \frac{1}{V_0} \sum_m \left[\frac{1}{2}(\mathcal{F}(Q_R) + \mathcal{F}(Q_L)) - \frac{1}{2}\mathcal{D}(Q_R, Q_L, \boldsymbol{S}) \right], \tag{12}$$

where V_0 is the volume at cell 0, $\mathcal{F} = \boldsymbol{F} \cdot \boldsymbol{S}$ is the directed flux through the area-weighted face direction, $\boldsymbol{S}$, and $\mathcal{D}$ represents artificial diffusion/upwinding terms. The numerical flux above is formulated for each of the m faces forming each control volume.

The numerical flux terms involve right and left reconstructed states using data from surrounding cells to form estimates of solution gradients. In this work we consider a linear reconstruction method of the form

$$\begin{aligned} Q_L &= Q_0 + \Delta r_{0m}^T \nabla Q_0, \\ Q_R &= Q_i + \Delta r_{im}^T \nabla Q_i, \end{aligned} \tag{13}$$

where $\Delta r_{0m} = r_m - r_0$ is the vector joining the centroid of cell 0 to the quadrature point on face m, and ∇Q_0 represents an estimate of the gradient in cell 0. We now examine various linear reconstruction schemes in which the only difference is in the method of computing the cell gradients, including constant, cell least squares, and nodal Green–Gauss methods, shown in Fig. 1a–c. Within the nodal Green–Gauss method, we also examine different methods of computing nodal values from surrounding cell-center values, including a new projection method.

3.1.1. Constant reconstruction

For the constant reconstruction scheme, we assume that the solution is constant in each cell, such that

$$\nabla Q_0 = 0. \tag{14}$$

This scheme is expected to be first order accurate and, therefore, has reduced value for practical CFD computations. Nonetheless, it serves as a useful baseline with which to compare other schemes. The computational stencil for the constant scheme is shown in Fig. 1a.

3.1.2. Cell least squares reconstruction

In the cell least squares gradient approximation, we seek a linear function, $\overline{Q}$, that minimizes the function

$$f(\nabla Q_0) = \sum_i w_i(\overline{Q}(r_i) - Q_i), \tag{15}$$

where w_i are weights of the least squares procedure and are typically inversely proportional to the distance between cell 0 and each surrounding cell, i. In other words, we seek to minimize the difference between some linear function and the discrete values of Q. In this work we perform the least squares procedure on the conserved variables directly. The form of $\overline{Q}$ we choose is

$$\overline{Q} = Q_0 + \Delta r_{0i}^T \nabla Q_0 \tag{16}$$

The solution to Eq. (22) for linear $\overline{Q}$ has a well-known analytic solution, which may be found elsewhere [17]. The gradients computed with the cell least squares method may be expressed as

$$\begin{aligned} \frac{\partial Q}{\partial x} &= \sum_i \alpha_{x,i}(Q_i - Q_0), \\ \frac{\partial Q}{\partial y} &= \sum_i \alpha_{y,i}(Q_i - Q_0), \\ \frac{\partial Q}{\partial z} &= \sum_i \alpha_{z,i}(Q_i - Q_0), \end{aligned} \tag{17}$$

where the α coefficients may be computed and stored in a pre-process step for a given grid. The local stencil for the least squares procedure should be large enough to avoid a singular system, but small enough to avoid unnecessary computational expense. Good results have been obtained with the stencil composed of all cell and node neighbors for a given cell, as shown in Fig. 1b.

3.1.3. Nodal Green–Gauss reconstruction

An alternate gradient estimation method for unstructured grids consists of a nodal Green–Gauss procedure. This procedure has several advantages over the cell least squares method, which will
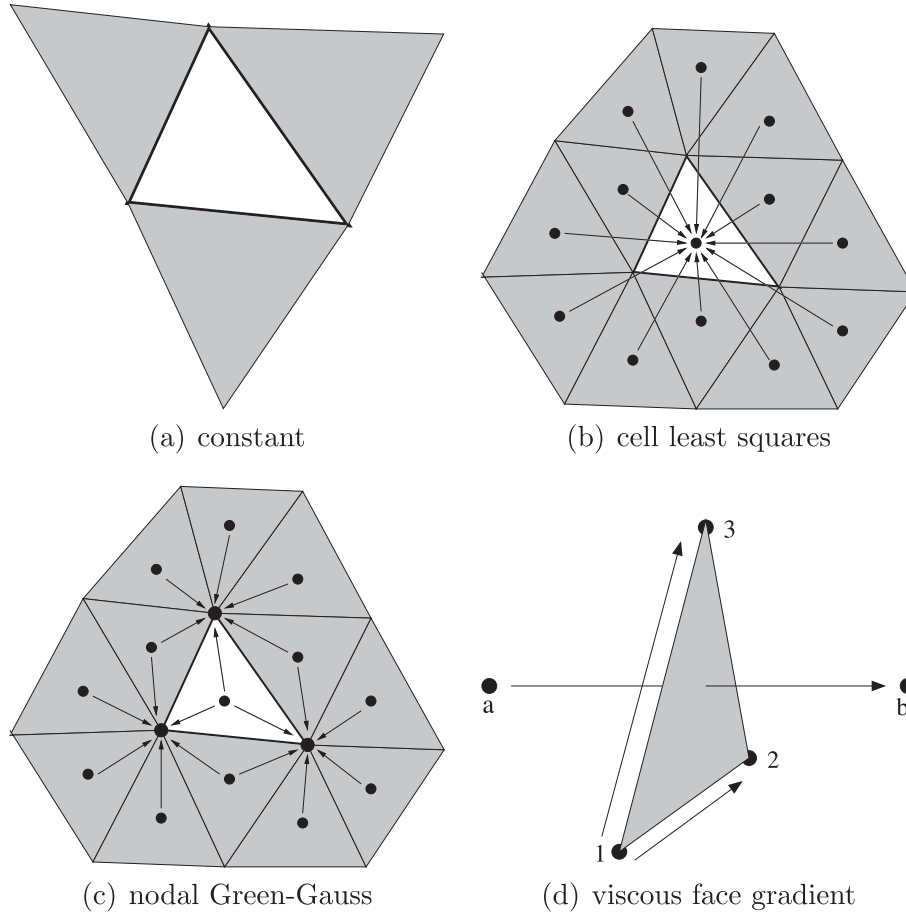
(a) constant

(b) cell least squares

(c) nodal Green-Gauss

(d) viscous face gradient

Fig. 1. Methods of gradient reconstruction for inviscid term discretization and face gradient approximation for viscous discretization.

be discussed below. The nodal Green–Gauss procedure involves estimating the gradient in a cell as

$$\nabla Q_0 = \frac{1}{V_0} \sum_m \widetilde{Q}_m \mathcal{S}_m, \tag{18}$$

where the summation is performed over the faces of each control volume surface with area vector $\mathcal{S}$. If the face is a quadrilateral, the face is first split into two triangles and treated as two faces. Here, $\widetilde{Q}_m$ is the average value of Q on the face, and may be computed as

$$\widetilde{Q}_m = \frac{1}{3}\left(Q_{m1}^{node} + Q_{m2}^{node} + Q_{m3}^{node}\right), \tag{19}$$

where $Q_{m1,2,3}^{node}$ represent the values of Q at the nodes comprising face m. Thus, the nodal Green–Gauss procedure involves first computing nodal values of Q from surrounding cell center data, followed by the trapezoidal integration procedure of Eq. (18).

There are several possible ways to compute the nodal values from surrounding cell-center data. We consider three methods. The first is referred to as the "nodal volume" scheme and involves a volume weighted average of the cell values j surrounding each node, i:

$$Q_i^{node} = \frac{\sum_j V_j Q_j}{\sum_j V_j}. \tag{20}$$

This scheme was used by Jameson and Vassberg in an earlier work [18].

The second method involves a least squares interpolation at each node and is referred to as the "nodal least squares" scheme.

This scheme is similar to the Laplacian scheme of Rausch et al. [19] and Holmes and Connell [3]. Instead of computing derivatives directly as for the cell least squares procedure described above, here we are concerned with interpolating data to the nodes. We minimize a function of the same form as Eq. (22), but this time define $\overline{Q}$ as

$$\overline{Q} = Q_i^{node} + \Delta r_{ij}^T \nabla Q_i^{node}, \tag{21}$$

where Q_i^{node} is the unknown nodal value for which we seek from surrounding cells, j. Incidentally, by solving for Q_i^{node}, we also solve for the gradient of Q at the node, but we do not store this information as we are only interested in the nodal value of Q. Solving this minimization problem leads to

$$Q_i^{node} = \sum_j \alpha_{ij} Q_j, \tag{22}$$

where the α_{ij} are now scalar weighting coefficients on the surrounding cell center values.

It is interesting to compare the storage and computational requirements of the nodal least squares scheme and the cell least squares scheme for a regular triangular mesh in two dimensions. In such a mesh, there are twice as many cells (2N) as there are nodes (N), excluding boundary effects. This means we must compute twice as many cell least squares problems as node least squares problems. In three dimensions, the ratio is even greater, around five or six for tetrahedra. Examining Fig. 1, the cell least squares stencil contains 12 cells, while the node least squares stencil contains six cells at each node. The storage requirements for cell least squares is then 48N floating point weight coefficients, since

each x- and y-derivative uses a separate coefficient. Since the node least squares method only requires a scalar weight for interpolation, the storage requirement is only $6N$. Of course, the nodal least squares requires the subsequent trapezoidal integration of Eq. (18), but this involves face areas that are already stored for the overall flux procedure. Also, the nodal scheme requires storage of the nodal values of Q, but again these values are needed anyway in the viscous flux discretization and do not represent additional storage. Therefore, the node least squares procedure is cheaper in terms of storage and computation than the cell least squares procedure in our framework. The savings are even greater in three dimensions.

The nodal least squares scheme and the nodal volume scheme are of a similar form and make use of a common stencil, shown in Fig. 1c. Later we show that the use of nodal least squares is critical to maintaining second order accuracy, while the nodal volume scheme degrades to first order. However, the nodal least squares scheme becomes highly unstable for high aspect ratio grids with curvature. For these types of grids we wish to devise a new nodal scheme that maintains second order accuracy and stability. We refer to this scheme as the "nodal projection" scheme. This scheme is similar to the approximate mapping scheme of Diskin and Thomas [20], but here again the goal is to obtain nodal values for use in a Green–Gauss integration procedure, not to obtain the gradient directly. Our method also differs from the method of Diskin and Thomas in the way in which we define the local coordinate system for the least squares procedure, and our method is formulated here in three dimensions.

The nodal projection method is designed for prismatic grids that are often used for capturing boundary effects near solid bodies. These grids are illustrated in Figs. 2 and 3 in two and three dimensions. The projected least squares method consists of a 2D least squares interpolation on a projection plane, followed by a 1D interpolation along the prismatic direction to obtain nodal values. First, the projection plane is defined as that plane which passes through the point midway between adjacent prismatic nodes (shown as the filled squares in Fig. 2) and minimizes the perpendicular distance to the cell-center locations of the surrounding cells. This plane is the orthogonal distance regression plane which passes through the adjacent cell-centers. These planes may be found by finding the minimum of the function

$$f(\boldsymbol{n}) = \sum_i [\boldsymbol{n} \cdot (\boldsymbol{r}_i - \boldsymbol{r}_m)]^2, \qquad (23)$$

where $\boldsymbol{n}$ is the unit normal of the regression plane, $\boldsymbol{r}_i$ are the position vectors of the surrounding cell centers, and $\boldsymbol{r}_m$ is the position vector of the location midway between adjacent nodes through
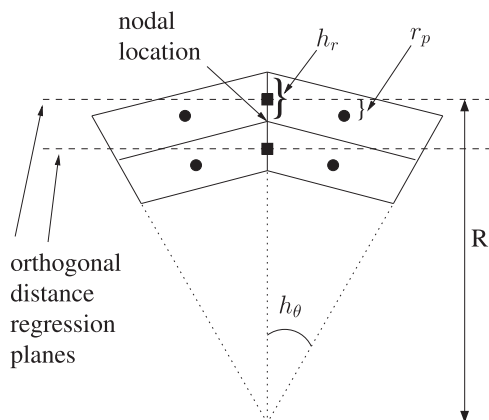

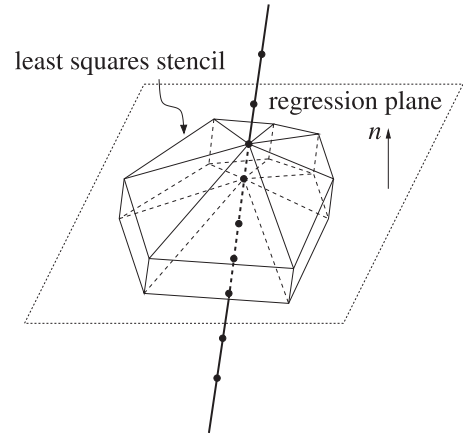**Fig. 2.** Illustration of projection technique to obtain nodal values in 2d.

Fig. 3. Illustration of projection technique to obtain nodal values in 3d.

which the regression plane passes (the filled squares). The function f may be equivalently expressed as a Rayleigh quotient

$$f(\boldsymbol{n}) = \frac{\boldsymbol{n}^T A \boldsymbol{n}}{\boldsymbol{n}^T \boldsymbol{n}}, \qquad (24)$$

where $A = M^T M$, and

$$M = \begin{bmatrix} x_1 - x_m & y_1 - y_m & z_1 - z_m \\ x_2 - x_m & y_2 - y_m & z_2 - z_m \\ \vdots & \vdots & \vdots \\ x_N - x_m & y_N - y_m & z_N - z_m \end{bmatrix}.$$

The Rayleigh quotient is minimized when $\boldsymbol{n}$ equals the eigenvector corresponding to the minimum eigenvalue of A. We can show that this eigenvector of A is equal to the singular vector M corresponding to the smallest singular value of M. Therefore, we only need the singular value decomposition (SVD) of M to find the normal $\boldsymbol{n}$ of the regression plane. The two largest singular values of M are two orthonormal vectors that lie within the regression plane. Denoting these two unit vectors as $\hat{\xi}$ and $\hat{\boldsymbol{\eta}}$ we now solve a two dimensional least squares problem in the projection plane of the form in Eq. (22), but using a new linear fitting function

$$\overline{Q} = Q_m + \hat{\xi}^T \Delta r_{mj} \frac{\partial Q}{\partial \hat{\xi}} + \hat{\boldsymbol{\eta}}^T \Delta r_{mj} \frac{\partial Q}{\partial \hat{\boldsymbol{\eta}}}, \qquad (25)$$

where Q_m is the value of Q at the filled square location in Fig. 2. Once all the filled square location values are obtained, a simple 1D interpolation is used to obtain the nodal values. This entire procedure is part of a pre-process step and may be distilled down to the convenient form of Eq. (22). As in the other nodal schemes, we use these nodal values in a Green–Gauss integration around each cell to obtain cell gradients.

In the projection process, essentially we assume that the cell values lie in a plane, when if fact we know that in general they do not. The error in making this assumption is minimized by finding the best fit plane through the stencil of cell-centers. Nonetheless, the error of the projection can be quantified by examining Fig. 2, which shows a simple curved grid with radius R, radial spacing h_r, tangential spacing h_θ, and projection distance, r_p. The projection error, E_p, can be expressed as

$$E_p = \frac{r_p}{h_r} = \frac{R\left(1 - \cos\frac{h_\theta}{2}\right)}{h_r} \approx \frac{Rh_\theta^2}{8h_r} = \frac{ARh_\theta}{8}, \qquad (26)$$

where r_p is the orthogonal projection distance. This result shows that the error in making the projection actually decreases with grid refinement at constant aspect ratio, $AR = R\, h_\theta/h_r$. This is what en-

ables the projection scheme to maintain second order accuracy and stability for curved grids as we will show in the results section.

3.2. Viscous terms

The discretization of the viscous terms uses a combination of nodal values reconstructed using any of the nodal methods of the previous section (nodal volume, nodal least squares, or nodal projection), and the primary cell-center values. Using a finite volume formulation, the spatial discretization for the viscous terms in Eq. (1) may be expressed as

$$\mathbf{\nabla} \cdot \boldsymbol{F}_v(Q, \nabla Q) \approx \frac{1}{V_0} \sum_m \mathcal{F}_v(\widetilde{Q}_m, \nabla \widetilde{Q}_m), \qquad (27)$$

where $\mathcal{F}_v = \boldsymbol{F}_v \cdot \boldsymbol{S}$ is the directed viscous flux through the area-weighted face direction on each face, m. Here, $\widetilde{Q}_m$ and $\nabla \widetilde{Q}_m$ are the independent variables and their gradients reconstructed at the quadrature point on face m.

Once the nodal values have been obtain with any of the methods of the previous section, the value of $\widetilde{Q}_m$ is obtained using Eq. (19). Referring to Fig. 1d, the value of $\nabla \widetilde{Q}_m$ may be obtained by solving the following system at each face:

$$\begin{bmatrix} \Delta x_{31} & \Delta y_{31} & \Delta z_{31} \\ \Delta x_{21} & \Delta y_{21} & \Delta z_{21} \\ \Delta x_{ba} & \Delta y_{ba} & \Delta z_{ba} \end{bmatrix} \begin{Bmatrix} \partial \widetilde{Q}_m / \partial x \\ \partial \widetilde{Q}_m / \partial y \\ \partial \widetilde{Q}_m / \partial z \end{Bmatrix} = \begin{Bmatrix} Q_{m3}^{node} - Q_{m1}^{node} \\ Q_{m2}^{node} - Q_{m1}^{node} \\ Q_b - Q_a \end{Bmatrix}. \qquad (28)$$

This method is similar to the node averaging schemes outlined by Diskin et al. [21].

3.3. Flux integration

Three dimensional grids with cells other than tetrahedra potentially exhibit non-planar faces. Both viscous and inviscid fluxes need to be integrated on these faces to at least the order of accuracy of the scheme. A commonly used method of integration over a quadrilateral face is to evaluate the flux at the face center (average of the four nodes comprising the face). However, our previous studies [12], as well as those of Delanaye and Liu [22,23], have advocated first dividing each quadrilateral face into two planar triangular faces, and then performing the integration at the centroid of each triangle. The two procedures, shown in Fig. 4, are examined in this work for their impact on solution accuracy.

4. Results

In this section, we highlight the results of systematic grid refinement studies with manufactured solutions for a variety of

(a) single pt. quadrature   (b) double pt. quadrature

Fig. 4. Flux quadrature strategies for non-planar faces.

mesh features common to high aspect ratio grids. We test inviscid and viscous algorithms for scalar and Navier–Stokes equations outlined in the previous section. Mesh features we examine include aspect ratio, mesh stretching, curvature, skewness, and non-planar faces. In all cases we implement exact Dirichlet conditions at all boundaries.

4.1. Aspect ratio

First, we examine the effects of aspect ratio on solution accuracy. For this case we use the same manufactured solution, shown in the bottom of Fig. 5. We fix the stretching ratio in the wall normal direction and systematically decrease the domain height, as shown in the top of Fig. 5. We define the domain aspect ratio as $AR = x_{ref}/y_{ref}$ and vary this to isolate aspect ratio effects. The solution parameter v in Eq. (30) is changed such that the 99% boundary layer thickness is captured as the domain height changes. For this test, we examine quadrilaterals only.

The results of this refinement test are shown in Fig. 6. Fig. 6a and b shows the effect of various discretizations at the inviscid and viscous limits, respectively, for domain aspect ratio $AR = 10^4$. At the inviscid limit, the constant reconstruction and Green–Gauss nodal volume reconstruction methods exhibit first order accuracy, while the cell least squares and Green–Gauss methods with either nodal least squares and nodal projection show second order accuracy with nearly identical results. Surprisingly, all nodal methods show second order accuracy at the viscous limit, including the nodal volume scheme which shows first order accuracy for the viscous terms. To investigate this behavior further, a range of Reynolds numbers are tested at $AR = 10^4$ for the nodal volume scheme, shown in Fig. 7. While not shown, the nodal projection scheme gives nearly identical results. As the regime transitions from viscous dominated to inviscid dominated, the first order behavior becomes apparent. This observation warrants further investigation, but is seen repeatedly in subsequent tests.

Fig. 6c and d show the effect of domain aspect ratio on the solution error at the inviscid and viscous limits, respectively, for the nodal least squares method. At both limits, the schemes show slightly less error for domain aspect ratio 10^0, but are then completely insensitive to increases in aspect ratio. Aspect ratio alone does not appear to impact solution accuracy. Rather, it is the degree of stretching that has a much larger impact, as will be seen in the next section.

A similar domain aspect ratio test is performed in three dimensions using the prismatic mesh and manufactured solution configuration shown in Fig. 8. The surface mesh consists of triangles with random perturbations of the nodal locations by 25% of the maximum spacing between nodes to avoid any fortunate error cancellations. The wall normal direction consists of the same stretching used in the previous 2D case. Manufactured solutions and source term derivation can become quite complex in three dimensions, even with automated symbolic manipulation tools. Therefore, a simple trigonometric manufactured solution has been used with a scaled z coordinate to enable domain aspect ratio scaling. The manufactured solution for density is

$$\begin{aligned} \rho(x,y,z) = \rho_0 &+ \rho_x \sin\left(\frac{\alpha_{\rho x} \pi x}{L}\right) + \rho_y \cos\left(\frac{\alpha_{\rho y} \pi y}{L}\right) \\ &+ \rho_z \sin\left(\frac{\alpha_{\rho y} \pi z^*}{L}\right) + \rho_{xy} \cos\left(\frac{\alpha_{\rho xy} \pi xy}{L^2}\right) \\ &+ \rho_{xz} \sin\left(\frac{\alpha_{\rho xz} \pi xz^*}{L^2}\right) + \rho_{yz} \sin\left(\frac{\alpha_{\rho yz} \pi yz^*}{L^2}\right), \end{aligned} \qquad (29)$$

where $z^* = z/z_{ref}$ is the z-coordinate scaled with the domain length in the z-direction, z_{ref}. This scaling allows the manufactured solution to maintain the same character as the domain is scaled in the z-direc-
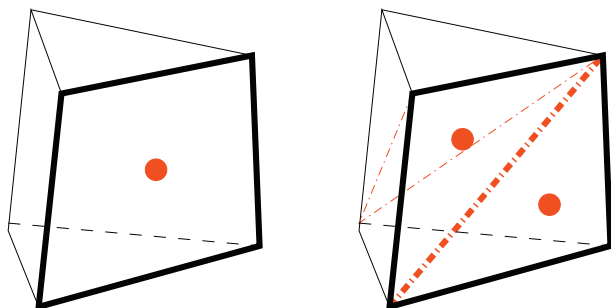
(a) $AR = 1$ (b) $AR = 2$ (c) $AR = 4$

Fig. 5. Scalar 2D test case to examine aspect ratio effects.

(a) various schemes, $Re \to \infty$, $AR = 10^4$ (b) various schemes, $Re \to 0$, $AR = 10^4$

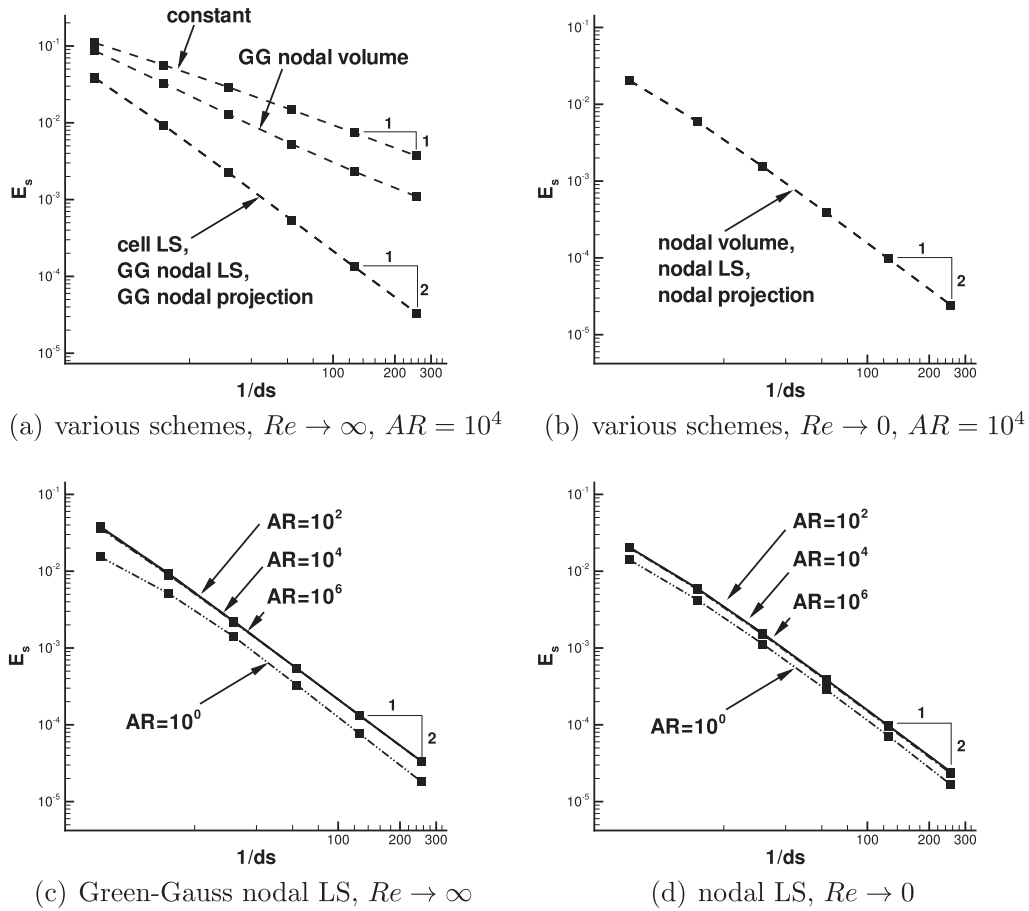(c) Green-Gauss nodal LS, $Re \to \infty$ (d) nodal LS, $Re \to 0$
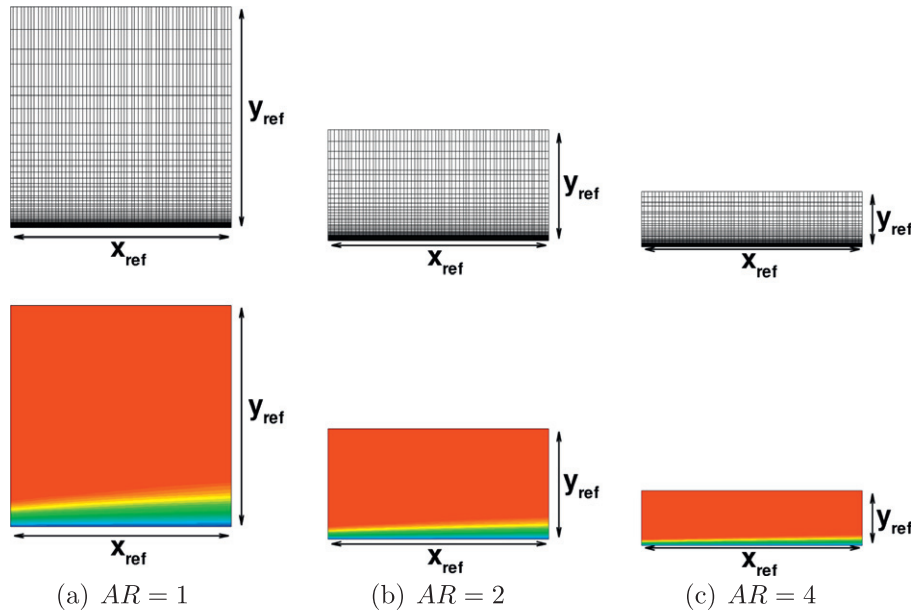
Fig. 6. Results of the aspect ratio test. Aspect ratio (*AR*) refers to the aspect ratio of the entire domain. (a) The order of accuracy of various schemes for $Re \to \infty$ and $AR = 10^4$. (b) The order of accuracy of various schemes for $Re \to 0$ and $AR = 10^4$. (c) The error from the Green–Gauss nodal least squares method at the inviscid limit. (d) All nodal schemes at the viscous limit.

tion. Similar solutions are generated for *u*, *v*, *w*, and *P*. Here, ρ_0 is the freestream value, and the ρ_* and α_* coefficients are arbitrarily chosen constants.

The results of the 3D aspect ratio test are shown in Fig. 9. Error in *x*-momentum using three domain aspect ratios is shown. For all cases the nodal least squares procedure was used for both the
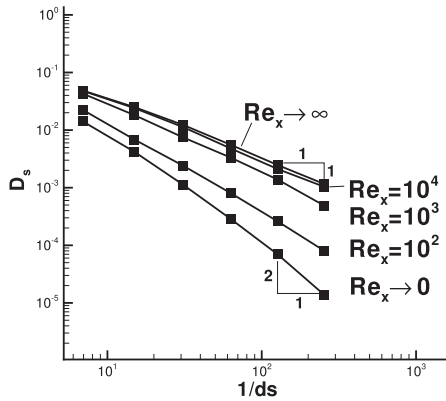
Fig. 7. Effect of Reynolds number on accuracy for the nodal least squares scheme, which is first order accurate for inviscid terms and second order accurate for viscous terms.

inviscid and viscous fluxes. Fig. 9a shows error convergence for $Re_x = 10^1$, while Fig. 9b shows error convergence for $Re_x = 10^4$. For the low Reynolds number case, the results show little sensitivity to aspect ratio, consistent with the 2D results. For the higher Reynolds number case, the results are somewhat surprising. There appears to be an optimal aspect ratio (around $AR = 10^3$), which produces the lowest error. Aspect ratios lower and higher than this displayed more error. Further investigation into this phenomenon

is warranted. Nonetheless, all aspect ratios at all Reynolds numbers exhibited second order accuracy, as expected.

4.2. Mesh stretching

Next, we examine the effects of mesh stretching in a direction normal to a wall. The meshes used for this test case are shown in Fig. 10, and include quadrilaterals, equilateral triangles, and right triangles. Uniform grids are produced and then stretched near the lower wall to capture regions of high gradients. For a given grid refinement case, the aspect ratio of the first cell off the wall is specified and held constant. Several such refinement cases are performed at various aspect ratios and Reynolds numbers for the scalar system in Eq. (2). The stretching is performed using geometric spacing such that the ratio of adjacent cell spacing is constant throughout the mesh, but the domain height is fixed at $y = 1$. Thus, as the aspect ratio of the wall cells increases, the stretching becomes more severe.

The manufactured solution used for this case, shown in Fig. 5 is similar to that used by Sun et al. [10], and has a boundary layer-like character:

$$\phi(x,y) = 1 - e^{\frac{-(y-y_0)}{\sqrt{v(x-x0)}}},\tag{30}$$

where v was chosen to obtain 99% boundary layer thickness at the upper boundary of the domain at $y = 1$.

The results of grid refinement tests for this case are shown in Fig. 11. The nodal least squares method is used with the Green–Gauss
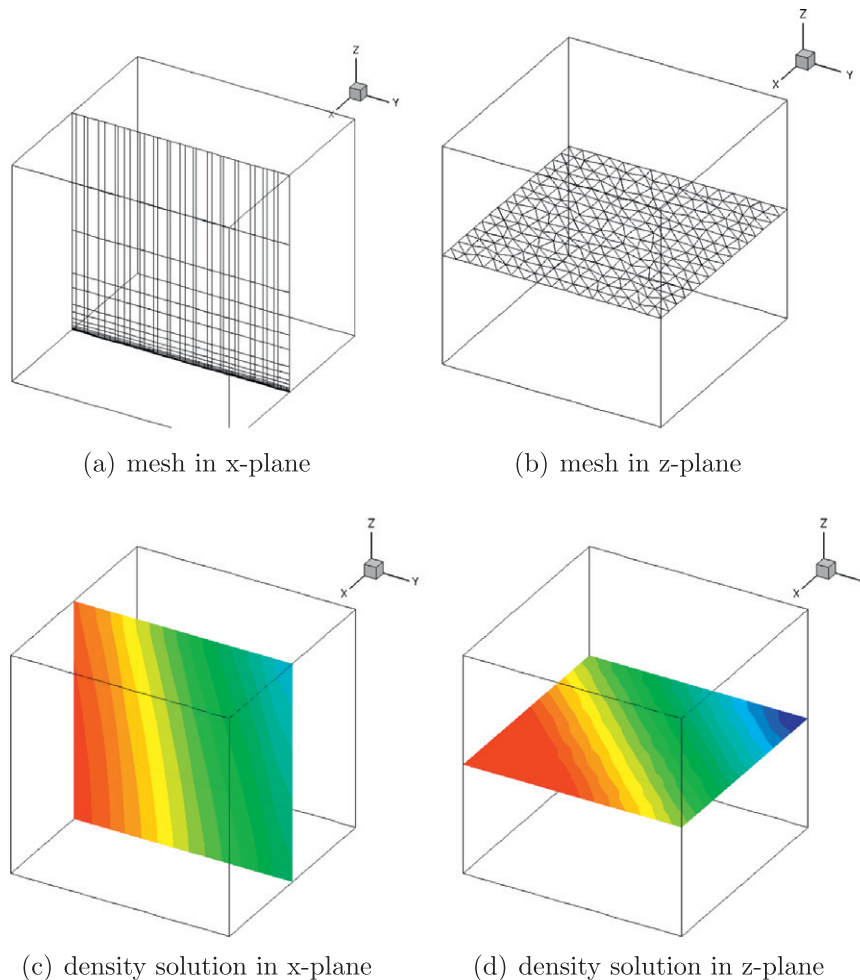

(a) mesh in x-plane

(b) mesh in z-plane

(c) density solution in x-plane

(d) density solution in z-plane

Fig. 8. Navier–Stokes 3D test case to examine aspect ratio effects.

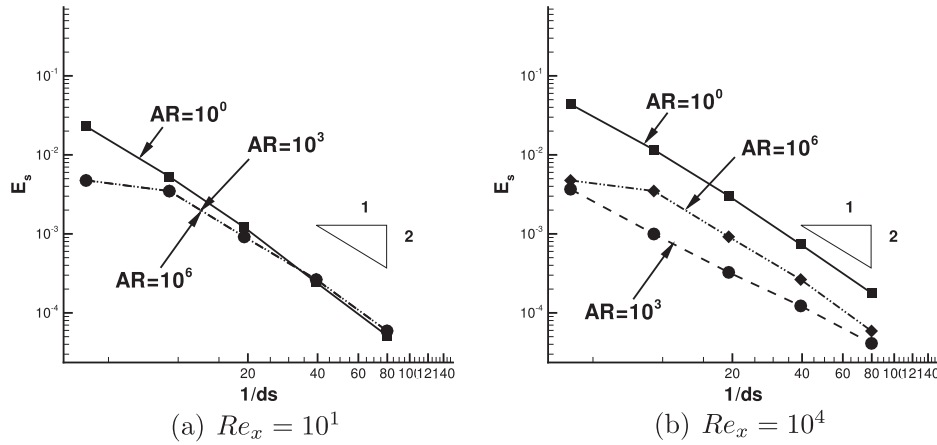(a) $Re_x = 10^1$ (b) $Re_x = 10^4$

Fig. 9. Aspect ratio effects for the 3d Navier–Stokes equations. Error in *x*-momentum shown using Green–Gauss nodal least squares for inviscid fluxes and nodal least squares for viscous fluxes.
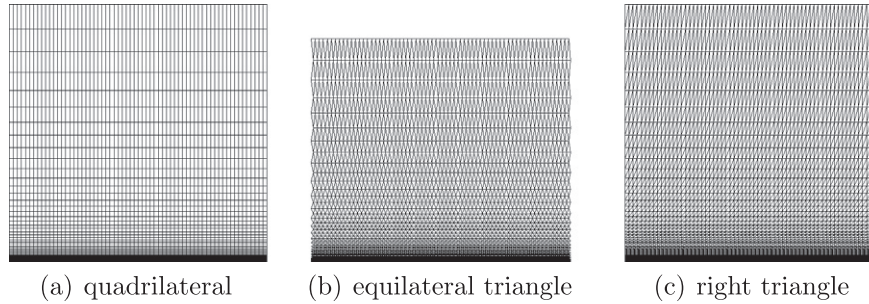

(a) quadrilateral   (b) equilateral triangle   (c) right triangle

Fig. 10. Grid types used to assess mesh stretching effects in 2D.

procedure for the inviscid fluxes and the face gradient procedure for the viscous fluxes. All cases show second order accuracy. Fig. 11a and b shows the effect of cell type for wall cell aspect ratio $AR = 10^4$ for the inviscid and viscous limits, respectively. At the inviscid limit, there is little difference among cell types. However, at the viscous limit, quadrilateral cells produce lower magnitude of error. This supports the notion that high aspect ratio prismatic grids near walls are best suited to capture viscous effects. Fig. 11c and d shows the effect of increased stretching (increasing wall cell aspect ratio) for the inviscid and viscous limits, respectively, for quadrilaterals. While not shown, the triangular grids perform similarly.

4.3. Curvature

Next, we examine the effects of curvature on accuracy and stability. For this case we use the 2D mesh in Fig. 12a, and the scalar manufactured solution in Fig. 12b. This solution has the polar coordinate form

$$\phi(r,\theta) = 1 - e^{\frac{-(r-r_0)}{\sqrt{\nu(\theta_0-\theta)}}}. \tag{31}$$

Again we choose ν such that we obtain 99% boundary layer thickness at a radial distance of $r = 1$, starting from the cylinder surface at $r = 0.5$. This solution is representative of boundary effects over curved geometry. The refinement is performed in a manner similar to the stretching test; for a particular refinement test, the domain size and aspect ratio of the first cell off the wall are kept fixed. This procedure was repeated for various wall cell aspect ratios, keeping the domain size fixed at $0.5 \leqslant r \leqslant 1$. By varying

the wall cell aspect ratio, we are in effect varying the curvature of the grid. Following the definition of Diskin et al. [21], the curvature induced deformation can be defined as

$$\Gamma = AR\frac{h_\theta}{2}, \tag{32}$$

where $AR = Rh_\theta/h_r$ is the cell aspect ratio, and h_θ is the tangential spacing. For a given refinement process, we choose AR to be constant and vary h_θ (and h_r). Therefore, the highest curvature grids are coarse meshes (large h_θ) and high aspect ratio (large AR). As a given grid is refined, the curvature decreases. This is a similar effect to the decrease in projection error in Eq. (26) with grid refinement.

The results of this test at the inviscid limit are shown in Fig. 13 for a variety of schemes and wall cell aspect ratios. All schemes show sensitivity to an increase in wall cell aspect ratio. This increase in error is likely due to increased stretching, similar to the previous stretching studies for flat grids. For these tests, six levels of refinement were used. Any missing data points for a refinement case indicate lack of convergence due to stability problems. This occurs in Fig. 13b for the cell least squares scheme for the $AR = 10^6$ coarse grids and in Fig. 13d for the Green–Gauss nodal least squares for all but the $AR = 10^2$ fine grids. The cell least squares scheme is mildly unstable, while the Green–Gauss nodal least squares scheme is highly unstable for even mild curvature. Neither the constant, Green–Gauss nodal volume, or Green–Gauss nodal projection schemes show any instability. However, of these three, the only scheme that is both stable and second order accurate for all levels of curvature tested was the Green–Gauss nodal projection scheme.

A comparison of various schemes at the inviscid limit is shown in Fig. 14 for $AR = 10^6$. This clearly shows the second order accuracy
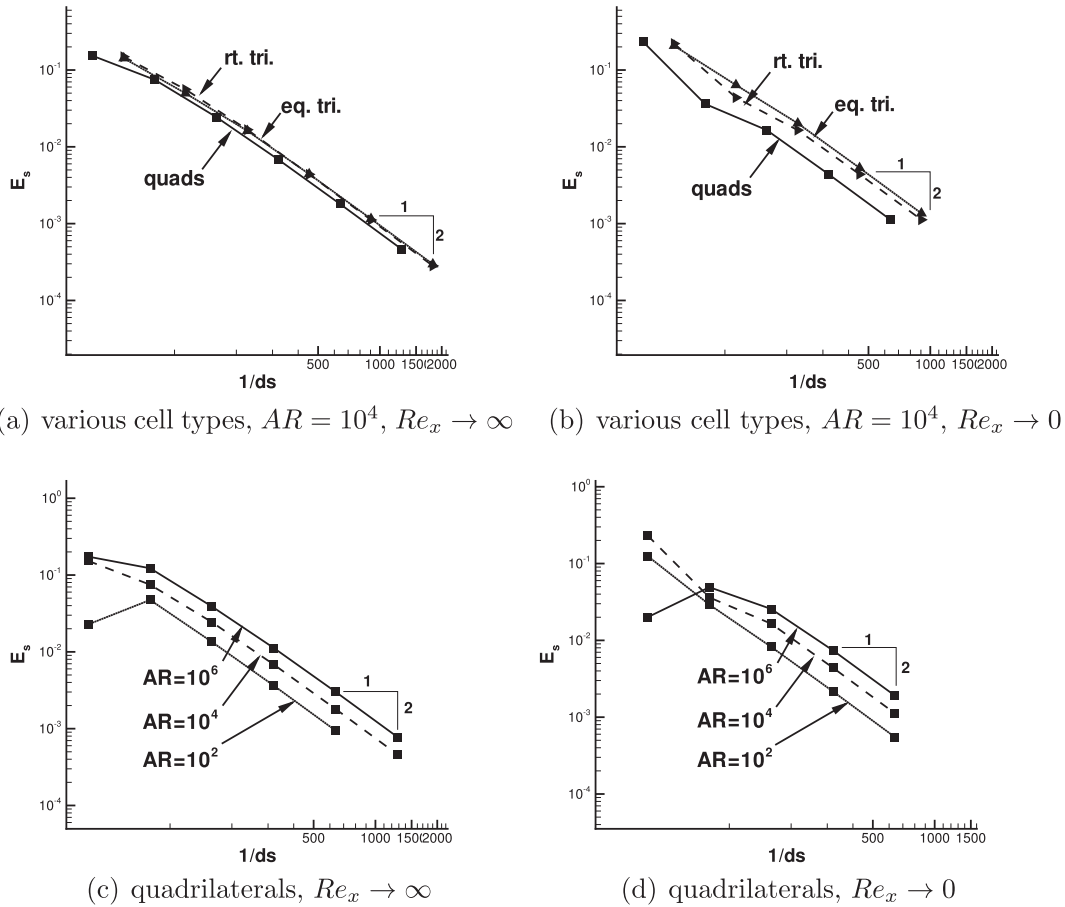
(a) various cell types, $AR = 10^4$, $Re_x \to \infty$ (b) various cell types, $AR = 10^4$, $Re_x \to 0$

(c) quadrilaterals, $Re_x \to \infty$ (d) quadrilaterals, $Re_x \to 0$

Fig. 11. Results of the mesh stretching tests using the nodal least squares method. Aspect ratio (AR) refers to the aspect ratio of the first cell off the wall. (a and b) Error for various cell types at $AR = 10^4$ at the inviscid and viscous limits. (c and d) The effect of mesh stretching at the inviscid and viscous limits.

(a) 2d curved mesh   (b) scalar manufactured solution
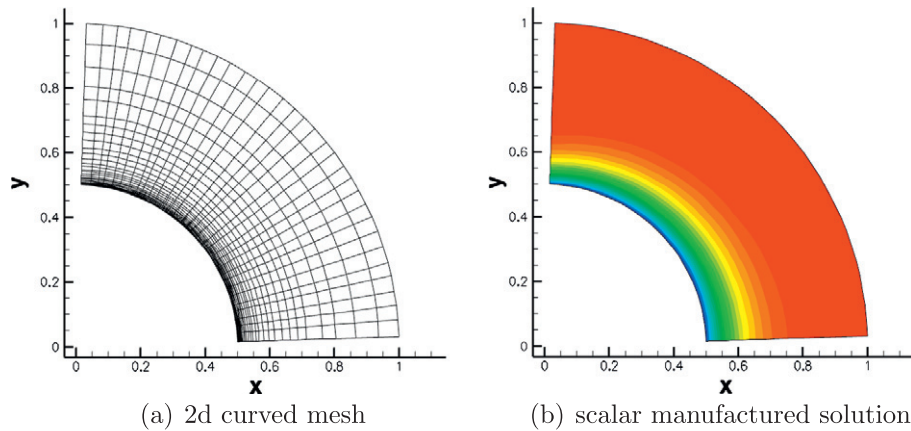
Fig. 12. Scalar 2D test case to examine curvature effects.

obtained by both the cell least squares (when stable) and the nodal projection schemes. Like the constant reconstruction scheme, the nodal volume scheme is first order accurate, but asymptotes to a significantly lower level of error.

A similar comparison for the viscous limit is shown in Fig. 15 for $AR = 10^2$, $AR = 10^4$, and $AR = 10^6$. No distinction between the various nodal methods for the viscous discretization can be made for all levels of wall cell aspect ratio. Interestingly, even the nodal least squares method, which led to severe instability in the inviscid terms, appears stable and accurate for the viscous terms. Consistent with previous tests, the viscous terms appear to be more forgiving for stability.

4.4. Skewness

Next, we examine the effects of grid skewness on solution accuracy for various discretizations. For this test we use the 2D mesh configuration in Fig. 16a, which is the same mesh used for testing domain aspect ratio, but skewed at a variable skew angle, σ. We also use the same scalar manufactured solution of Eq. (30), shown in Fig. 16b for this mesh. We systematically vary the skew angle and measure the solution error for various schemes.

The results of the skew angle test for the inviscid limit are shown in Fig. 17 for various levels of skewness. The results clearly show once again the first order accuracy of the Green–Gauss nodal
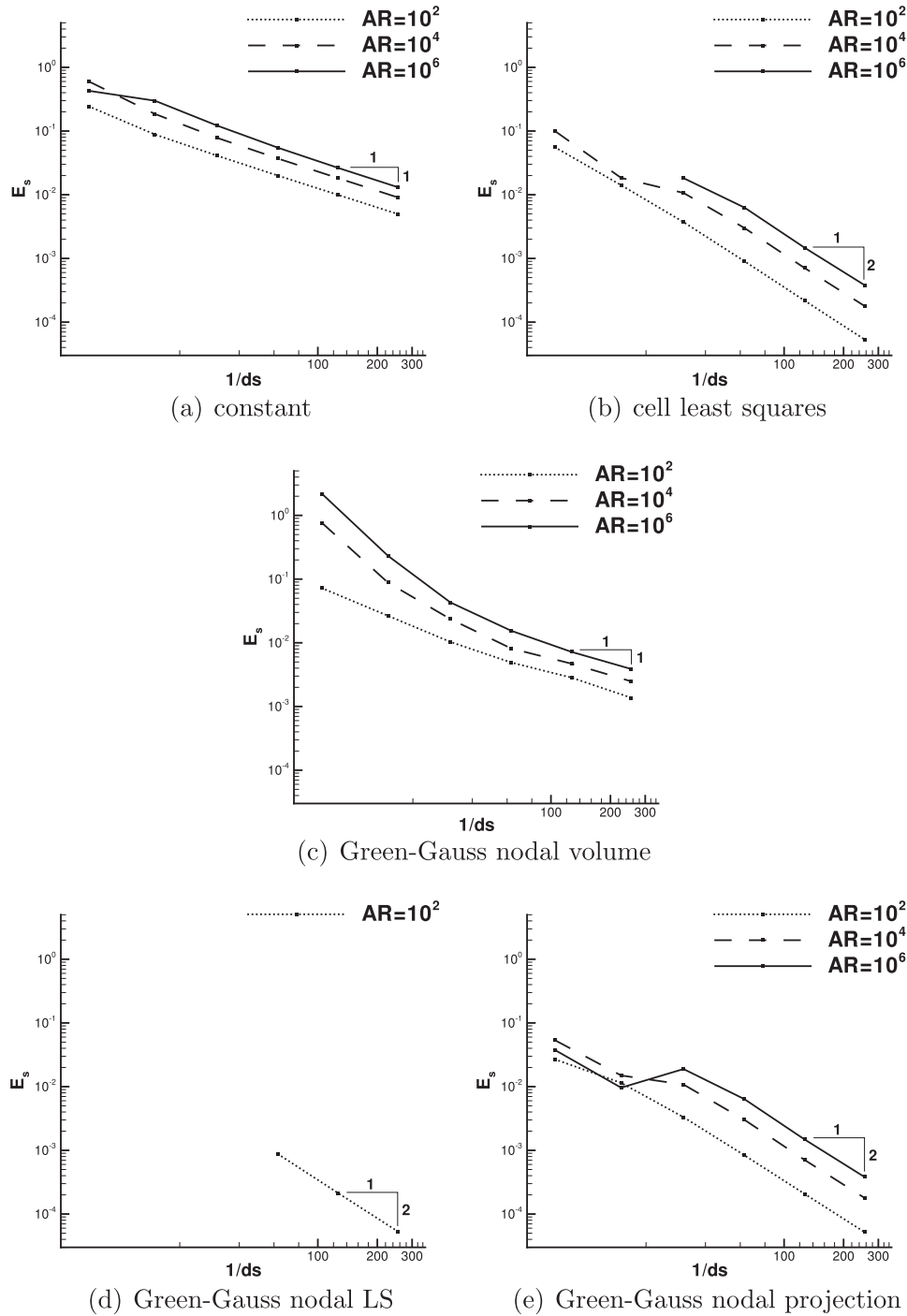
(a) constant

(b) cell least squares

(c) Green-Gauss nodal volume

(d) Green-Gauss nodal LS

(e) Green-Gauss nodal projection

Fig. 13. Error of various reconstruction schemes at the inviscid limit, $Re \rightarrow \infty$, for varying levels of curvature.

volume scheme, while the nodal projection scheme retains sharp second order accuracy. Additionally, the nodal volume scheme appears more sensitive to skewness at very high skew angle. Overall, for moderate levels of skewness, both schemes show little sensitivity to skew angle. An important feature of the nodal projection scheme highlighted by this case is its ability to automatically detect the correct projection plane for skewed meshes by minimizing the orthogonal distances of the stencil points. For purely skewed meshes with no curvature such as for this case, there is no projection error because all stencil points lie in a plane, which is correctly identified by the SVD procedure.

Fig. 18, shows a similar result for the viscous limit. Once again, the nodal volume scheme shows sharp second order accuracy for

the viscous terms, which was not the case for the first order accurate inviscid terms. Furthermore, the viscous discretization appears even less sensitive to skew angle than the inviscid terms, even for very high skew angle.

4.5. Non-planar faces

In order to test the effect of single versus double point quadrature discussed in Section 3.3 on solution accuracy, we construct a randomly perturbed grid, shown in Fig. 19. The grid nodes are perturbed a distance up to 25% of the largest spacing between adjacent nodes to produce non-planar faces. The same manufactured solution described in Eq. (29) and shown in Fig. 8 is used.
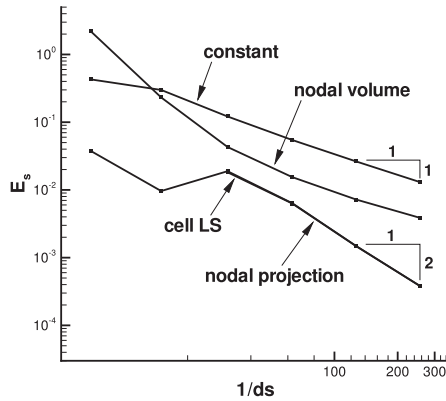
Fig. 14. Comparison of various reconstruction schemes at the inviscid limit, $Re \rightarrow \infty$, for $AR = 10^6$.
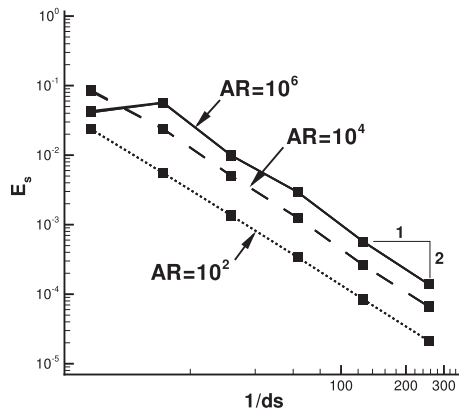

Fig. 15. All nodal schemes at the viscous limit, $Re \rightarrow 0$, for varying levels of curvature.

Fig. 17. Comparison of the Green–Gauss nodal volume and Green–Gauss nodal projection schemes at the inviscid limit, $Re \rightarrow \infty$.

Fig. 18. Comparison of the nodal volume and nodal projection schemes at the viscous limit, $Re \rightarrow 0$.

Results of this test are shown in Fig. 20. Error in the x-momentum equation is shown for four Reynolds numbers using both single point and double point (triangulated) quadrature. For all Reynolds numbers the single point quadrature produces first order errors, while the double point quadrature produces second order errors. In both cases, the error appears to increase in magnitude as the Reynolds number increases, but to a greater degree for the single point quadrature. This seems to indicate that the inviscid terms are more sensitive to the choice of quadrature method than the viscous terms.
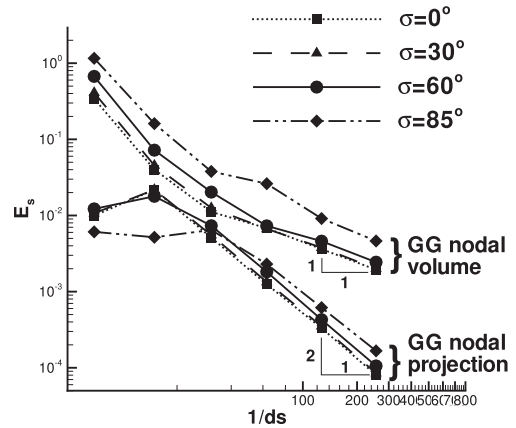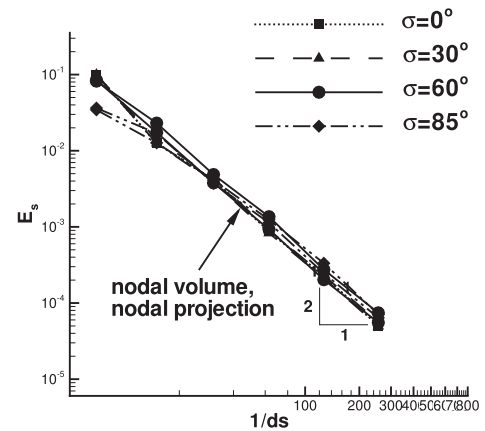
5. Conclusions

Unstructured grid schemes have achieved mainstream use for practical CFD computations, but the discretizations remain sensitive to mesh quality. In this work, we have examined the accuracy of convection–diffusion systems, including the 3D Navier–Stokes equations, as a function of unstructured grid parameters such as the grid aspect ratio, stretching ratio, curvature, skewness and
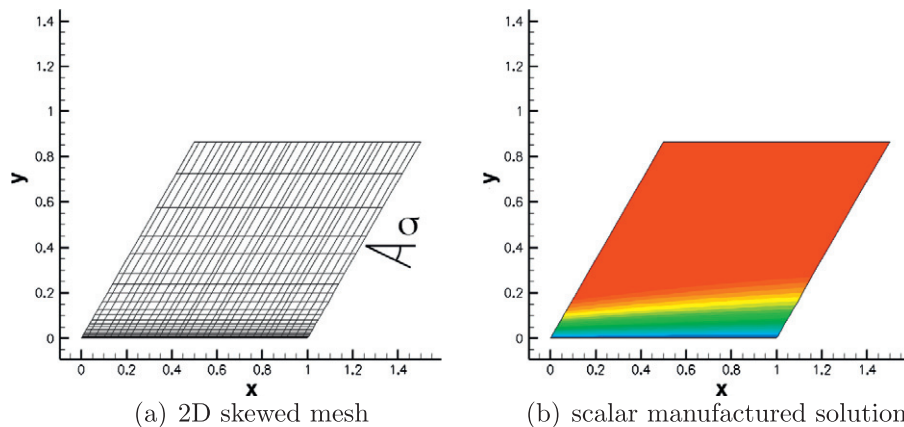

(a) 2D skewed mesh

(b) scalar manufactured solution

Fig. 16. Scalar 2D test case to examine skewness effects.

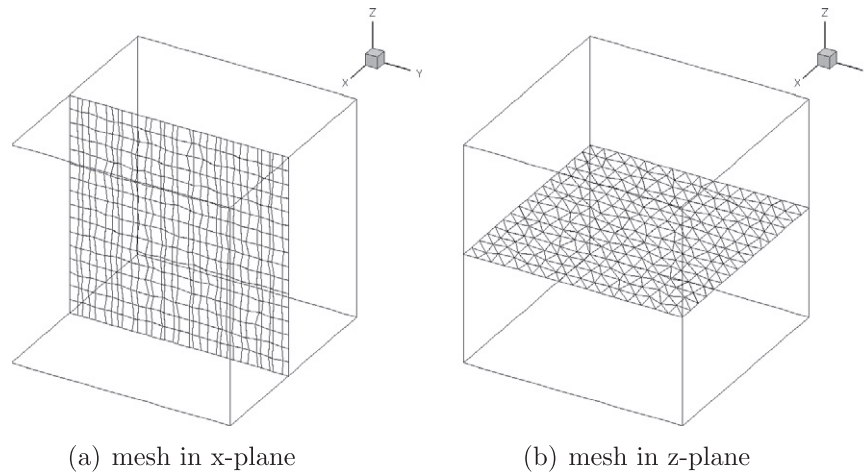(a) mesh in x-plane   (b) mesh in z-plane

Fig. 19. Mesh and manufactured Navier–Stokes solution to examine the effects of non-planar face treatment in 3D.
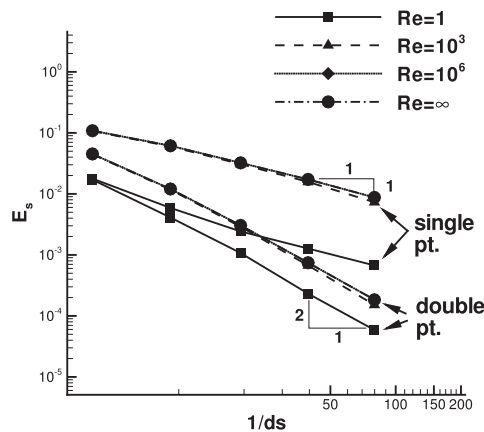

Fig. 20. Error convergence of single point versus double point (triangulated) quadrature for the 3D Navier–Stokes equations. x-Momentum equation shown for various Reynolds numbers.

non-planar faces (in 3D). The Method of Manufactured Solutions (MMSs) is used to systematically study these effects for a number of inviscid and viscous flux discretization schemes. An observation regarding the use of MMS is the importance of treating the source term discretization with an order of accuracy that is equal to or greater than that employed for the inviscid and viscous flux terms. Moreover, in addition to benchmarking the order of accuracy of the discretization methods, the MMS approach is also useful in cataloguing the stability behavior of the schemes.

Specific inviscid discretization schemes that have been tested here include constant reconstruction, cell-least squares and a variety of nodal-based Green–Gauss reconstruction techniques. In the latter instance, the nodal values are reconstructed using nodal least squares, volume-weighting, and a new nodal projection scheme. The important conclusion of the study is that the newly developed nodal projection scheme is shown to be a robust discretization method for the inviscid terms that preserves second-order accuracy for all the conditions tested. The most challenging mesh configuration for many second-order schemes is the high curvature case, for which the nodal projection scheme maintains second order accuracy and stability for all levels of curvature, while the other schemes either revert to first-order accuracy or encounter stability issues. A second conclusion is related to cells with non-planar faces in three-dimensions. Non-planar faces require the use of a double-point quadrature on triangulated facets to maintain second order accuracy, while a single quadrature point at the face center reduces the accuracy to first order.

An advantage of the nodal schemes is that they also facilitate the treatment of the viscous gradients on the cell-face. Viscous discretizations based on face gradients derived from nodal values are shown to be more forgiving in terms of accuracy and stability than the inviscid gradient reconstruction schemes. For example, the nodal volume scheme leads to first order accuracy when used in a Green–Gauss gradient procedure for inviscid terms, but shows second order accuracy when used to compute face gradients for viscous terms. Similarly, the nodal least squares method is highly unstable for even moderate levels of curvature at the inviscid limit, but shows no such instabilities in the viscous limit. Finally, the impact of the single point quadrature for non-planar faces is also more prominent at higher Reynolds numbers, indicating greater sensitivity in the inviscid terms.

Future work will focus on the effect of mesh features for unstructured high-order methods such as the Discontinuous Galerkin (DG) methods that are under development. Commensurate high-order source term discretization in the MMS procedure is expected to be critical for accurate evaluation of such schemes. The framework we have developed in this work should prove useful for understanding the stability and accuracy characteristics of these methods.

Acknowledgements

References

[1] Mavriplis D, Venkatakrishnan V. A unified multigrid solver for the Navier–Stokes equations on mixed element meshes. Int J Comput Fluid Dyn 1997;8:247–63.
[2] Mavriplis DJ. Unstructured mesh discretizations and solvers for computational aerodynamics. In: AIAA paper 2007-3955, AIAA 18th CFD Conf., Miami; 2007.
[3] Holmes D, Connell S. Solution of the 2D Navier–Stokes equations on unstructured adaptive grids. In: AIAA paper 89-1392, AIAA 9th CFD Conference, Washington, DC; 1989.

[4] Diskin B, Thomas J. Comparison of node-centered and cell-centered unstructured finite-volume discretizations: inviscid fluxes. In: AIAA paper 2010-1079, AIAA 48th ASM, Orlando; 2010.

[5] haselbacher GPA, McGuirk J. Finite volume discretization aspects for viscous flows and mixed unstructured grids. AIAA J 1999;37:177–84.

[6] Roache P. Code verification by the method of manufactured solutions. Trans ASME 2002;124:4–10.

[7] S. Pautz, Verification of transport codes by the method of manufactured solutions: the attila experience. Technical report LA-UR-01-1487, Los Alamos (NM); 2001.

[8] Roy C. Review of code and solution verification procedures for computational simulation. J Comput Phys 2005;205:131–56.

[9] Luke E, Hebert S, Thompson D. Theoretical and practical evaluation of solver-specific mesh quality. In: AIAA paper 2008-0934, AIAA 46th aerospace sciences meeting, Reno, NV; 2008.

[10] Sun H, Darmofal D, Haimes R. On the impact of triangle shapes for boundary layer problems using high-order finite element discretization, In: AIAA paper 2010-0542, AIAA 48th aerospace sciences meeting, Orlando, FL; 2010.

[11] Svard M, Gong J, Nordstrom J. An accuracy evaluation of unstructured node-centered finite volume methods. NIA report 2005-04; 2005.

[12] Katz A, Sankaran V. Mesh quality effects on the accuracy of Euler and Navier–Stokes solutions on unstructured meshes. In: Technical report, 6th International conference on computational fluid dynamics, St. Petersburg, Russia; 2010.

[13] Diskin B, Thomas J. Accuracy analysis for mixed-element finite-volume discretization schemes. NIA report 2007-08, National Institute of Aerospace; 2007.

[14] Giles M. Accuracy of node-based solutions on irregular meshes. Lect Notes Phys 1989;323:273–7.

[15] Wendroff B. Supraconvergence in two dimensions. Technical report LA-UR-95-3068, Los Alamos; 1995.

[16] Despres B. Lax theorem and finite volume schemes. Math Comput 2003;73:1203–34.

[17] Katz A. Meshless methods for computational fluid dynamics. PhD thesis, Stanford University; 2009.

[18] Jameson A, Vassberg J. A vertex–centroid (V–C) scheme for the gas–dynamics equations. In: Technical report, International conference on CFD, Kyoto (Japan); 2000.

[19] Rausch R, Batina J, Yang H. Spatial adaptation of unstructured meshes for unsteady aerodynamic flow computations. AIAA J 1992;30:1243–51.

[20] Diskin B, Thomas J. Accuracy of gradient reconstruction on grids with high aspect ratio. NIA report 2008-12, National Institute of Aerospace; 2008.

[21] Diskin B, Thomas J, Nielsen E, Nishikawa H. Comparison of node-centered and cell-centered unstructured finite-volume discretizations. Part 1: Viscous fluxes. In: AIAA paper 2009-0597, AIAA 47th aerospace sciences meeting, Orlando, FL; 2009.

[22] Delanaye M, Liu Y. Quadratic reconstruction finite volume schemes on 3D arbitrary unstructured polyhedral grids. In: AIAA paper 1995-3259, AIAA 14th computational fluid dynamics conference, Norfolk, VA; 1999.

[23] Liu Y, Vinokur M. Exact integrations of polynomials and symmetric quadrature formulas over arbitrary polyhedral grids. J Comput Phys 1998;140:122–47.